

Improving resolution of superlens based on solid immersion mechanism

Zhanlei Hao(郝占磊), Yangyang Zhou(周杨阳), Bei Wu(吴贝), Yineng Liu(刘益能), and Huanyang Chen(陈焕阳)
Citation: Chin. Phys. B, 2023, 32 (**6**): 064211. DOI: 10.1088/1674-1056/ac8726
Journal homepage: http://cpb.iphy.ac.cn; http://iopscience.iop.org/cpb

What follows is a list of articles you may be interested in

Near-field multiple super-resolution imaging from Mikaelian lens to generalized Maxwell's fish-eye lens

Yangyang Zhou(周杨阳) and Huanyang Chen(陈焕阳)
Chin. Phys. B, 2022, 31 (**10**): 104205. DOI: 10.1088/1674-1056/ac5d34

Internal and near-surface fields for a chiral sphere under arbitrary laser beam illumination

Bi-Da Su(苏必达), Ming-Jun Wang(王明军), Yue Peng(彭月), Su-Hui Yang(杨苏辉), Hua-Yong Zhang(张华永)
Chin. Phys. B, 2019, 28 (**6**): 064210. DOI: 10.1088/1674-1056/28/6/064210

Super-resolution imaging via sparsity constraint and sparse speckle illumination

Pengwei Wang(王鹏威), Wei Li(李伟), Chenglong Wang(王成龙), Zunwang Bo(薄遵望), Wenlin Gong(龚文林)
Chin. Phys. B, 2018, 27 (**7**): 074202. DOI: 10.1088/1674-1056/27/7/074202

Superscattering-enhanced narrow band forward scattering antenna

Hu De-Jiao (胡德骄), Zhang Zhi-You (张志友), Du Jing-Lei (杜惊雷)
Chin. Phys. B, 2015, 24 (**10**): 104202. DOI: 10.1088/1674-1056/24/10/104202

Low threshold fiber taper coupled rare earth ion-doped chalcogenide microsphere laser

Li Chao-Ran (李超然), Dai Shi-Xun (戴世勋), Zhang Qin-Yuan (张勤远), Shen Xiang (沈祥), Wang Xun-Si (王训四), Zhang Pei-Qing (张培晴), Lu Lai-Wei (路来伟), Wu Yue-Hao (吴越豪), Lv She-Qin (吕社钦)
Chin. Phys. B, 2015, 24 (**4**): 044208. DOI: 10.1088/1674-1056/24/4/044208

SPECIAL TOPIC — Celebrating the 100th Anniversary of Physics Discipline of Xiamen University

Improving resolution of superlens based on solid immersion mechanism

Zhanlei Hao(郝占磊)[†], Yangyang Zhou(周杨阳)[†], Bei Wu(吴贝), Yineng Liu(刘益能)[‡], and Huanyang Chen(陈焕阳)[§]

Institute of Electromagnetics and Acoustics and Department of Physics, College of Physical Science and Technology, Xiamen University, Xiamen 361005, *China*

(Received 7 May 2022; revised manuscript received 27 July 2022; accepted manuscript online 5 August 2022)

Super-resolution imaging with superlens has been one of the fundamental research topics. Unfortunately, the resolution of superlens is inevitably restrained by material loss. To address the problem, we introduce the solid immersion mechanism into the slab superlens and the cylindrical superlens. The proposed solid immersion slab superlens (SISSL) and the solid immersion cylindrical superlens (SICSL) can improve the resolution by converting evanescent wave to propagating wave using high refractive index materials. From the perspective of applications, the cylindrical superlens with finite cross section and the ability of magnification or demagnification has more advantages than the slab superlens. Therefore, we focus on demonstrating analytically the super-resolution imaging of SICSL. Due to the impedance mismatching caused by solid immersion mechanism, the whispering gallery modes (WGMs) are excited between SICSL and the air interface. We clarify the excitation conditions of WGMs and analyze their influence on the imaging quality of SICSL. The SISSL and SICSL may pave a way to apply in lithography technique and real-time biomolecular imaging in future.

Keywords: super-resolution imaging, material loss, solid immersion cylindrical superlens, whispering gallery modes

PACS: 42.40.Lx, 77.22.Gm, 42.79.Bh, 42.55.Sa **DOI:** 10.1088/1674-1056/ac8726

1. Introduction

Resolution, an important parameter of distinguishing the object details in optical imaging systems, has been extensively studied in science and engineering. However, the Abbe diffraction limit tells us that the resolution of conventional optical imaging systems is always limited to around half a wavelength, and it stems from that the evanescent waves carrying the detailed information decays rapidly and cannot reach the far field.[1,2] In recent years, many efforts have been made to improve the imaging resolution. For example, the scanning near-field optical microscopy uses a probe to capture evanescent waves near the objects.[3] Later on, Pendry theoretically proposed perfect lens that can produce ideal diffraction-free images, which utilizes the negative refractive index materials to restore the evanescent waves.[4] Following the concept of perfect lens, the superlens has been realized in metamaterials,[5–11] metals,[12,13] surface plasmonons,[14] and hyperbolic metamaterials.[15,16] At the same time, the hyperlens[17–21] as far-field super-resolution lens was also designed by hyperbolic metamaterials which can convert the near-field evanescent waves to the far-filed propagating waves. The cylindrical and spherical hyperlenses have been manufactured in a similar way.[22,23] However, the superlens and hyperlens face the challenges of insurmountable manufacturing and material loss, which seriously hinder the practical applications and further development of the superlens and hyperlens.[24–28] Solid immersion lens (SIL) as another super-resolution lens was widely studied due to the easy preparation and low loss.[28–32] The SIL, utilizing the positive high refractive index materials to convert the evanescent waves to propagating waves, achieves the super-resolution imaging with higher magnification and numerical aperture than ordinary lens. So far, various SILs have been fabricated by natural materials[28,33,34] and novel metamaterials.[35,36] As a well-developed imaging method, SIL has been widely applied to lithography technique[37] and data storage.[38] At the same time, solid immersion mechanism provides more chance to improve the resolution of imaging systems.

In this work, we combine the solid immersion mechanism with slab superlens and cylindrical superlens, and propose solid immersion slab superlens (SISSL) and cylindrical superlens (SICSL). Solid immersion mechanism provides a new solution to the problem since the superlens system with material loss has the unsatisfied resolution. We make use of the transfer matrix method (TMM)[39] to analyze the transmission function of SISSL. The results verify that SISSL can transfer more evanescent wave components with higher wave vectors into imaging in contrast to the conventional superlens system at the same loss level. For the applications and practicability, we focus on the super-resolution imaging of the whole

[†]These authors contributed equally to this work.
[‡]Corresponding author. E-mail: lyn610@xmu.edu.cn
[§]Corresponding author. E-mail: kenyon@xmu.edu.cn

© 2023 Chinese Physical Society and IOP Publishing Ltd

or a part of SICSL, which similarly applies the advantages of solid immersion mechanism to convert evanescent wave to propagating wave on the image point and to improve the resolution. We also verify analytically the super-resolution performance of SICSL. The analytical results of super-resolution imaging agree well with the numerical results. In addition, due to the impedance mismatching between SICSL and the air interface, the whispering gallery modes (WGMs)[11] are excited and affect the imaging quality. We clarify the relation between the resolution and exciting WGMs by solving the eigen equations of SICSL. In addition, the proposed SISCL has a certain bandwidth and no aberration under the condition of no exciting WGMs, which is a significant advantage compared to the conventional solid immersion lenses.

2. Results and discussion

It is well known that a perfect lens can form perfect imaging by restoring all evanescent wave components at the imaging point, as shown in Fig. 1(a). We plot the lens system in x–y plane and the perfect lens slab is centered at $x = 0$, $y = 0$. The perfect lens can focus light from a point source ($x = -d$, $y = 0$) to another point ($x = d$, $y = 0$). In wave optics, all the incident waves can be considered as a superposition of plane waves with different k components in different directions. For simplicity, we only consider the transverse electric field (E_z, H_x, H_y),

$$E(x,y,t) = \sum_{k_y} E(k_y) \exp(\mathrm{i}k_x x + \mathrm{i}k_y y - \mathrm{i}wt)\, \boldsymbol{z}, \tag{1}$$

where k_x and k_y are the components of the wave vectors in x and y directions. According to the dispersion relation, $k_0^2 = k_x^2 + k_y^2$ ($k_0 = 2\pi/\lambda$ is the free-space wavenumber), if k_y is larger than k_0, k_x becomes a purely imaginary number, which means that this electromagnetic wave component exponentially decays along the x-direction. For ease of clarification, we divide the slab lens system into four layers from left to right as layer 1, 2, 3, and 4 respectively, as shown in Fig. 1(a). To verify the imaging performances of the lens system, the transmission function,[6] which describes the amplification ratio of evanescent field amplitudes with respect to each normalized plane-wave number k_y/k_0 components, from layer 1 to 4 for different k_0 components is calculated at the operating wavelength $\lambda = 2d$. For a perfect lens, it will be enhanced exponentially for all larger k components (the red solid curve in the log scale plot), as shown in Fig. 1(b). However, when material loss (e.g., a small imaginary part for the permittivity ε_2 of 0.0004i) is considered, only part of evanescent wave components can be restored at the image position. Therefore, there is a maximum transmission coefficient. When the k_y/k_0 component keeps on increasing, it will decay rapidly as shown by the transmission curve (see the green solid curve in Fig. 1(b)). In this case, the perfect lens becomes superlens, and it thereby becomes a challenge that the loss affects the resolution for the whole optical imaging superlens system. Here, to circumvent the challenge, we propose a valid method, solid immersion mechanism, to improve the imaging performance of superlens with small loss, e.g., 0.0004i. From Fig. 1(b), we can find that high-k evanescent wave components make a more valuable contribution towards the imaging quality with the increase of the slab material perturbation δ. Obviously, high index materials transfer evanescent waves with high-k components into the imaging point to improve the resolution of the superlens gradually when the slab material perturbation δ increases from 1 to 9. The normalized wave number k_y/k_0 for the peak of transmission function curve shifts from a small value to a large one, as depicted in Fig. 1(b). To further explore the relationship between the peak in transmission function and the degree of refractive index mismatching, we calculate the value of each peak in the transmission function for different material perturbations ranging from 1 to 9 and the results are described in Fig. 1(c). The results demonstrate that solid immersion mechanism improves the imaging resolution of the superlens system.

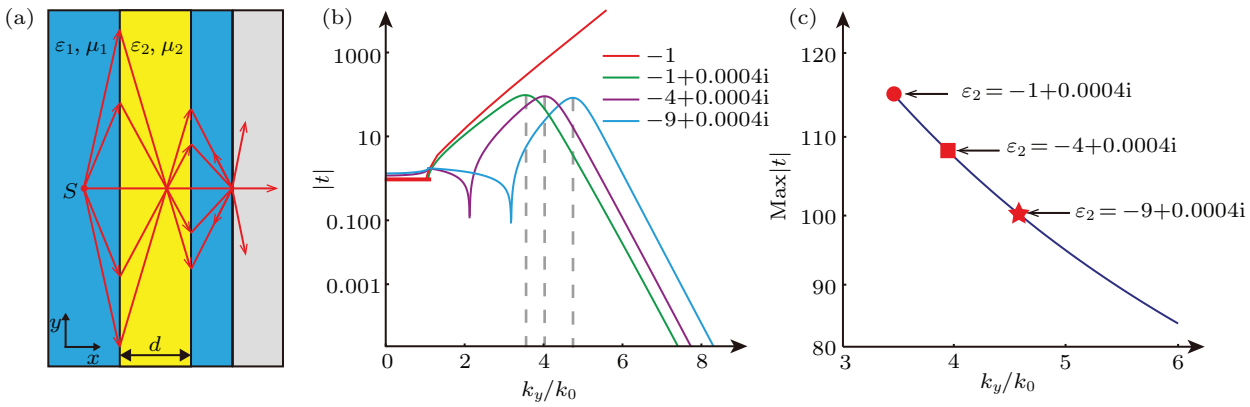


Fig. 1. Schematic of SISSL and transmission functions for a SISSL system from left (medium 1, with different values of permittivity) to right (air background). (a) A slab superlens with a thickness of d (permittivity $\varepsilon_2 = -\delta + 0.0004\mathrm{i}$, permeability $\mu_2 = -1$) is immersed in medium 1 (permittivity $\varepsilon_1 = \delta$, permeability $\mu_1 = 1$). The right part is air. (b) Comparisons of transmission functions for the superlens with four different permittivities ε_2. (c) The peak position in each transmission function for the superlens with respect to different values of permittivity ε_1 and ε_2 where the material perturbation δ increases from 1 to 9, and the corresponding peaks in (b) are also marked.

The results in Fig. 1 demonstrate that the SISSL can collect more high-order wave vector evanescent wave components information at the imaging points to improve the resolution of the superlens system. However, the cross section of slab superlens is infinite length, which greatly limits applications. By the method of transformation optics,[40–43] one can easily design a cylindrical superlens.[4,6,44] The advantage of this transformation is that it not only makes the superlens system have finite cross-sectional size, but also makes the superlens system have the ability of magnification or demagnification imaging. Therefore, the cylindrical superlens is one of the best choices for super-resolution imaging to overcome the diffraction limit from both the perspective of application and practicality. Figure 2(a) shows a particular radial coordinate transformation from a virtual space $(r',\ \theta',\ z')$ to a physical space $(r,\ \theta,\ z)$.[5,44] A cylindrical superlens is obtained by the following transformation:

$$r' = \begin{cases} \dfrac{c}{a}r, & 0 < r \le a, \\ \dfrac{b^2}{r}, & a < r \le b, \\ r, & b < r, \end{cases} \tag{2}$$

where a and b are the inner and outer radii of the cylindrical superlens, respectively. The continuity of endpoint at $r = a$ is considered, hence $c = b^2/a$. Besides, we can follow the folded mapping function[5] described by Eq. (1) to obtain the material parameters of the cylindrical superlens, where $0 < r \le a$ as the region 1,

$$\varepsilon_{r1} = \mu_{r1} = 1, \quad \varepsilon_{\theta 1} = \mu_{\theta 1} = 1, \quad \varepsilon_{z1} = \mu_{z1} = b^4/a^4; \tag{3}$$

$a < r \le b$ as the region 2,

$$\varepsilon_{r2} = \mu_{r2} = -1, \quad \varepsilon_{\theta 2} = \mu_{\theta 2} = -1, \quad \varepsilon_{z2} = \mu_{z2} = -b^4/r^4; \tag{4}$$

and $b < r$ as the region 3,

$$\varepsilon_{r3} = \mu_{r3} = 1, \quad \varepsilon_{\theta 3} = \mu_{\theta 3} = 1, \quad \varepsilon_{z3} = \mu_{z3} = 1. \tag{5}$$

Obviously, region 2 has both negative permittivity and permeability, and it is the cylindrical version of a slab superlens. To further investigate the imaging properties of the SICSL, we verify analytically the imaging performance. It is well known that the radial wave equation (transverse electric (TE) polarization) in cylindrical coordinate system can be written as

$$r^2 \frac{\mathrm{d}^2 E_z}{\mathrm{d}r^2} + r\frac{\partial E_z}{\partial r} + \left(k^2 r^2 - m^2\right) E_z = 0, \tag{6}$$

where $k = nk_0$, $k_0 = 2\pi/\lambda$ is the free-space wave number, n is the refraction index profile and m is an integer number. For the cylindrical superlens, we can obtain the general solution of the wave equation at different locations according to Eqs. (3)–(5) as follows:

for region 1, $0 \le r \le a$,

$$E_z^1 = \sum_{m=-\infty}^{\infty} \left(A_m J_m \left(\frac{k_0 b^2 r}{a^2} \right) + B_m Y_m \left(\frac{k_0 b^2 r}{a^2} \right) \right) \mathrm{e}^{\mathrm{i}m\theta}; \tag{7}$$

for the region 2, $a < r \le b$,

$$E_z^2 = \sum_{m=-\infty}^{\infty} C_m J_m \left(\frac{k_0 b^2}{r} \right) \mathrm{e}^{\mathrm{i}m\theta}; \tag{8}$$

for the region 3, $b < r$,

$$E_z^3 = \sum_{m=-\infty}^{\infty} \left(D_m J_m (k_0 r) + E_m Y_m (k_0 r) \right) \mathrm{e}^{\mathrm{i}m\theta}, \tag{9}$$

where J_m is the mth-order Bessel function and Y_m is the mth-order Neumann function. A_m, B_m, C_m, D_m, and E_m are the corresponding coefficients.

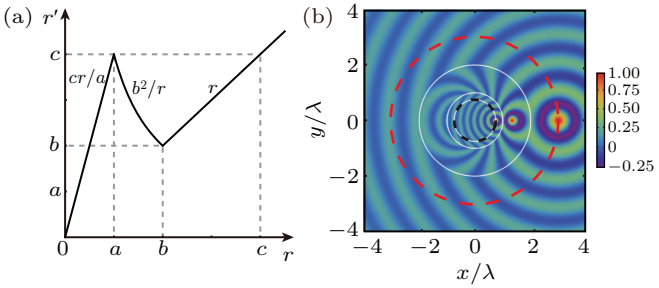


Fig. 2. Design of the cylindrical superlens. (a) The folded-geometry mapping function in the radial direction. (b) The simulated electric field pattern (E_z) for a line source of $\lambda = 1$ near a cylindrical superlens with $a = 1$, $b = 2$, and $c = 4$, the dashed circles denote the positions for the line source (black dotted line) and the image point (red dotted line).

The slab superlens and cylindrical superlens are essentially consistent, and they have similar imaging properties. The radial folded mapping can directly project the field of virtual space to physical space in the cylindrical superlens. According to the electromagnetic parameters of cylindrical superlens, the background material ($r > b$) of the superlens system is air, the middle part ($a < r < b$) is a negative refractive index material, and the inner core material of $r < a$ is a high refractive index medium with quadruple refractive index relative to air. Similar to the slab superlens, by placing the line current source at different positions inside the cylindrical superlens, it will be imaged outside of the superlens system with different field patterns. For ease of illustration, we consider electric field solely polarized in z direction (E_z polarization), and calculate analytically the imaging characteristics of the proposed cylindrical superlens. When the location of the line source satisfies $0 \le r_0 \le a^2/b$, the cylindrical superlens only forms an image at region 1 of the lens. When the line source r_0 is located between a^2/b and a, two perfect duplicates of the line source are obtained at the middle and outside layers of the cylindrical superlens, respectively. For example, when the line source is placed at $r_0 = a(b+c)/2c$, we calculate the electric field pattern of imaging, as shown in Fig. 2(b). It clearly shows that there are two different images located at $2b^2/(b+c)$ (region 2) and $(b+c)/2$ (region 3). The wavelength of the image

outside the cylindrical superlens is significantly amplified by four times compared with the inner core line source.

Similarly, the cylindrical superlens has the ability to overcome the diffraction barrier, and their imaging resolution is also inevitably restrained by the material loss. As we all know, the cylindrical perfect lens can produce a perfect imaging. However, when the material loss is introduced into the cylindrical superlens system, only part of the evanescent wave components can be recovered at the imaging position outside the superlens system. A very small material loss will cause the resolution of the superlens system to decrease rapidly or even exceed the diffraction limit 0.5λ. To further verify the super-resolution imaging of the cylindrical superlens, we analytically calculate the normalized electric field intensity $|E_z|^2$ and full width at half maxima (FWHM) of the cylindrical superlens system with material loss of 0.002i and 0.0008i at different wavelengths, as shown in Figs. 3(a), 3(b) and 3(d), 3(e). For the convenience of explanation, we define a common factor $\tau = -\kappa^2 + \xi\,\mathrm{i}$ (κ is a constant and ξ is the material loss). The permittivity of the cylindrical superlens with loss satisfies $\varepsilon'_{z1} = \kappa^2\varepsilon_{z2}\varepsilon'_{z2} = -\tau\varepsilon_{z2}\varepsilon'_{z3} = \kappa^2\varepsilon_{z3}$. The cylindrical superlens is also divided into four layers from inside to outside as layer 1, 2, 3, and 4, respectively, where the boundaries are at $r = a$, b, x_0 (the image point). Figures 3(a) and 3(d) show respectively the normalized electric field intensity $|E_z|^2$ of the cylindrical superlens with $\tau = -1 + 0.002\mathrm{i}$ and $\tau = -1 + 0.0008\mathrm{i}$, and the relative FWHM in the vertical direction at $x_0 = (b+c)/2$ and $-b < y_0 < b$ at wavelengths of 0.20 and 0.50. In the figures, the red curves represent the normalized electric field intensity $|E_z|^2$ at the imaging plane and the relative FWHM 0.55λ and 0.40λ of the imaging point are marked on the red curve, respectively. To improve the resolution of the cylindrical superlens with material loss, the solid immersion mechanism is introduced into the cylindrical superlens, which becomes a SICSL. Here, we choose a SICSL with $\tau = -2 + 0.002\mathrm{i}$ and $\tau = -2 + 0.0004\mathrm{i}$ as examples to explore the super-resolution imaging. Based on Eqs. (7)–(9), we obtain the normalized electric field intensity $|E_z|^2$ of the SICSL with $\tau = -2 + 0.002\mathrm{i}$ and $\tau = -2 + 0.0004\mathrm{i}$, and the relative FWHMs of the SICSL are respectively 0.45λ and 0.26λ at wavelengths of 0.20 and 0.50, as shown in Figs. 3(b) and 3(e). By comparing the FWHMs at $\lambda = 0.20$ and $\lambda = 0.50$, the FWHMs of SISCL with material loss of 0.002i and 0.0008i are respectively reduced by 0.10λ and 0.14λ compared to the superlens system, which indicates that SISCL has a smaller imaging resolution. Besides, we compare the transmission coefficients $\eta = |E_z^i|/|E_z^s|$ between SICSL and the cylindrical superlens at wavelengths of 0.20 and 0.50, where $|E_z^s|$ is the electromagnetic field amplitude of the point source component ($x = 0.75$, $y = 0$) and $|E_z^i|$ is the electromagnetic field amplitude of the transmitted component. It reveals that the more high-order evanescent wave components contribute to the imaging resolution of the SISCL (red solid line) compared to the cylindrical superlens (black solid line), as shown in Figs. 3(c) and 3(f), resulting in improvement of the imaging resolution in SISCL compared with the superlens system. Therefore, we analytically demonstrate that the solid immersion mechanism can improve the resolution of the cylindrical superlens with material loss.

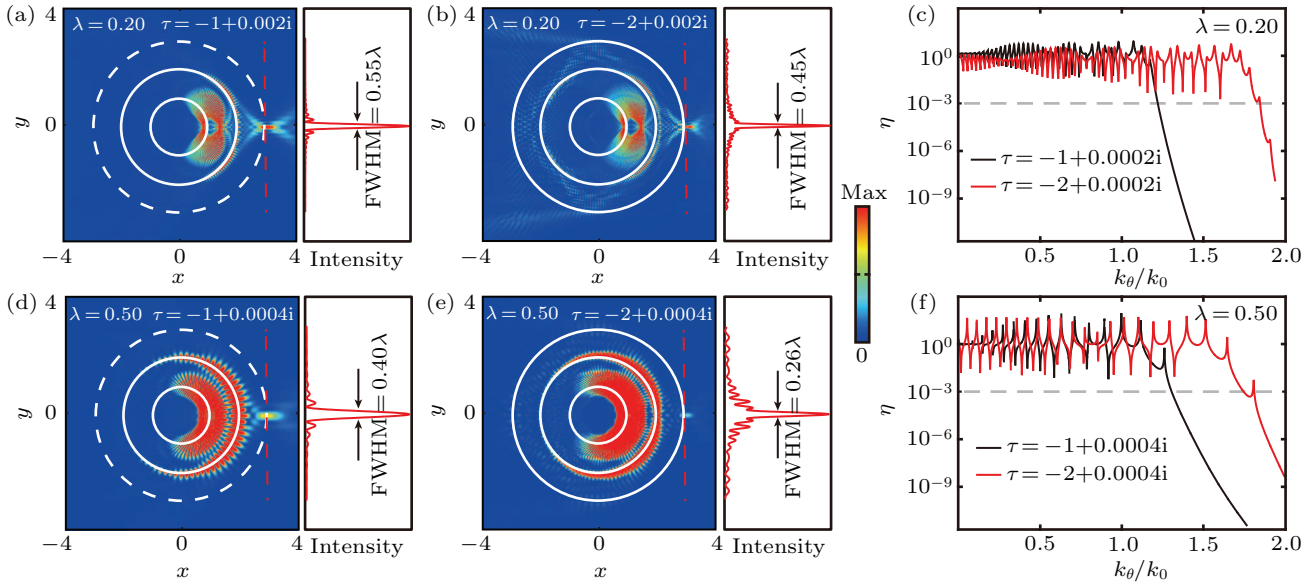


Fig. 3. The normalized electric field intensity $|E_z|^2$ of SICSL (left) with $a = 1$, $b = 2$, $c = 4$, and FWHM curve located at the dashed red line (right) at (a) $\lambda = 0.20$, $\tau = -1 + 0.002\mathrm{i}$, (b) $\lambda = 0.20$, $\tau = -2 + 0.002\mathrm{i}$, (d) $\lambda = 0.50$, $\tau = -1 + 0.0004\mathrm{i}$, and (e) $\lambda = 0.50$, $\tau = -2 + 0.0004\mathrm{i}$. Comparison of transmission coefficient $\eta = |E_z^i|/|E_z^s|$ for SISCL with (c) $\tau = -1 + 0.002\mathrm{i}$ (black curve in a log scale plot) and $\tau = -2 + 0.002\mathrm{i}$ (red curve in a log scale plot), (f) $\tau = -1 + 0.0004\mathrm{i}$ (black curve in a log scale plot) and $\tau = -2 + 0.0004\mathrm{i}$ (red curve in a log scale plot). $k = 2\pi/\lambda$ is free-space wave number, and $k_\theta = m/r_i$, r_i is the radial of the image position and m represents the azimuthal momentum number.

Due to the impedance mismatching between SICSL and air interface, WGMs are excited at the specific wavelengths and damage the super-resolution imaging quality of SICSL. In fact, when the electromagnetic wave propagates from SICLS into the air, the WGMs excited on the superlens are constrained by the eigen equations. By solving the eigen equation of the SICSL, we obtain the eigenfrequencies of the WGMs. Next, we will analytical calculate the excited WGMs in SICSL with $\tau = -2 + 0.0004\mathrm{i}$ ($\kappa^2 = 2$). By solving two separate 2D Helmholtz equations of air and SICSL, we can obtain the solution form as follows:

$$\psi_m(r) = \begin{cases} \alpha_m J_m(\kappa k_0 r)\, \mathrm{e}^{\mathrm{i}m\theta}, & r \le x_0, \\ \beta_m H_m^{(1)}(k_0 r)\, \mathrm{e}^{\mathrm{i}m\theta}, & r > x_0, \end{cases} \tag{10}$$

where α_m, β_m are the complex coefficients, and $x_0 = cr_0/a$ is the location of the imaging point. With the continuous boundary conditions of electric and magnetic fields at $r = x_0$, we can obtain the eigen equation which determines the eigenfrequencies as follows:

$$\frac{\alpha_m}{\beta_m} = \frac{H_m^{(1)}(k_0 x_0)}{J_m(\kappa k_0 x_0)}, \quad \frac{J'_m(\kappa k_0 x_0)}{J_m(\kappa k_0 x_0)} = \frac{1}{\kappa}\frac{H'^{(1)}_m(k_0 x_0)}{H_m^{(1)}(k_0 x_0)}, \tag{11}$$

where $H_m^{(1)}$ denotes the first Hankel function of the mth-order. The above characteristic equation is a transcendental equation and can only be solved numerically. According to Eq. (11), we analytically calculate all the relative FWHM of the imaging point in the air background whose wavelength is from 0.2 to 1.5 with a step of 0.01 under $\tau = -2 + 0.0004\mathrm{i}$, as shown in Fig. 4(b) (red circles). The relative FWHM of the cylindrical superlens with $\tau = -1 + 0.0004\mathrm{i}$ is also simultaneously plotted as comparison, as shown by black circles. We can clearly find that the excitation wavelength of WGMs is consistent with the super-resolution failure wavelength of SICSL. For example, when $m = 23$, we obtain the corresponding eigenwavelength of WGMs $\lambda \approx 0.99$ by solving Eq. (11). At the same wavelength, we analytically calculate the electric field patterns $|E_z|^2$ of the imaging utilizing Eqs. (7)–(9). Figure 4(a) shows the corresponding result, where the WGMs with $m = 23$ are also excited. The red curve represents the normalized electric field intensity $|E|^2$ at the imaging plane and the relative FWHM of SICSL is 1.36λ, which is far larger than the diffraction limit of 0.5λ. The results indicate that the WGMs damage the super-resolution imaging of SICSL. Although the FWHM results of SICSL have no obvious change trend, we can clearly find that it is always slightly smaller than the control group of $\tau = -1 + 0.0004\mathrm{i}$ when the WGMs is not excited. Besides, the WGMs depend greatly on the geometry of the resonator cavity, and we can optimize the geometry of the cavity to reduce or eliminate the excitation mode of WGMs. Therefore, we could conclude that the imaging resolution of SICSL is affected at the wavelength of WGM excitation. The imaging resolution of SICSL with material loss in the air background can be improved when the WGMs are not excited.

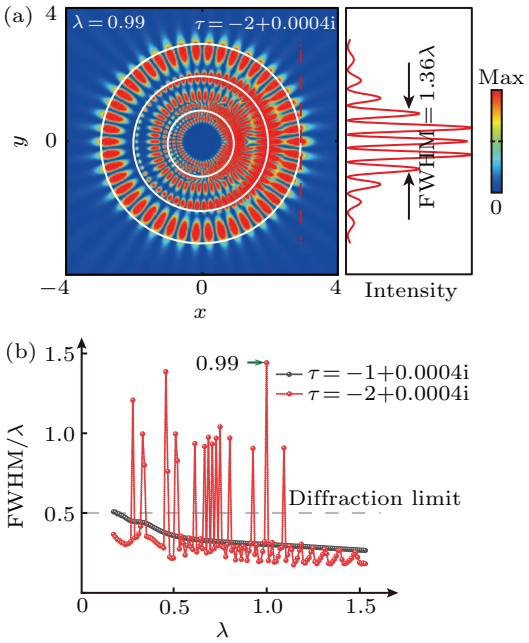


Fig. 4. (a) The WGMs of normalized electric field intensity $|E_z|^2$ (left) and the FWHM curve located at the dashed red line (right) at $\lambda = 0.99$. (b) The relative FWHM of $\tau = -1 + 0.0004\mathrm{i}$ (the black circle) and $\tau = -2 + 0.0004\mathrm{i}$ (the red circle) with increasing wavelength from 0.2 to 1.5 with a step length of 0.01.

3. Conclusion

In summary, we combine the solid immersion mechanism with the slab and cylindrical superlens system to design the SISSL and SICSL, and analytically prove that the solid immersion mechanism can improve the imaging resolution of the superlens system by restoring more evanescent wave components at the image point. However, due to the impedance mismatch between SICSL and air interface, the phenomenon of WGMs is generated in SICSL. We make clear the conditions of WGMs excitation in the SICSL, and analytically demonstrate that the WGMs can damage the super-resolution imaging of SICSL. These findings could contribute in multiple perspectives to our further understanding of high-resolution imaging, and may provide more possibility for lithography technique[37] and real-time imaging.[23]

Acknowledgements

Project supported by the National Key Research and Development Program of China (Grant No. 2020YFA0710100), the National Natural Science Foundation of China (Grant Nos. 92050102 and 11874311), and the Fundamental Research Funds for the Central Universities (Grant Nos. 20720220033 and 20720200074).

References

[1] Hell S W 2007 *Science* **316** 1153

[2] Huang B, Wang W Q, Bates M and Zhuang X 2008 *Science* **319** 810
[3] Betzig E and Trautman J K 1992 *Science* **257** 189
[4] Pendry J B 2000 *Phys. Rev. Lett.* **85** 3966
[5] Chen H Y, Chan C T and Sheng P 2010 *Nat. Mater.* **9** 387
[6] Yan M, Yan W and Qiu M 2008 *Phys. Rev. B* **78** 125113
[7] Salandrino A and Engheta N 2006 *Phys. Rev. B* **74** 075103
[8] Soukoulis C M and Wegener M 2011 *Nat. Photon.* **5** 523
[9] Zhang S, Park Y S, Li J, Lu X C, Zhang W L and Zhang X 2009 *Phys. Rev. Lett.* **102** 023901
[10] Xu T, Agrawal A, Abashin M, Chau K J and Lezec H J 2013 *Nature* **497** 470
[11] Zhou Y Y, Hao Z L, Zhao P F and Chen H Y 2022 *Phys. Rev. Appl.* **17** 034039
[12] Ma C B and Liu Z W 2010 *Appl. Phys. Lett* . **96** 183103
[13] Ma C B, Escobar M A and Liu Z W 2011 *Phys. Rev. B* **84** 195142
[14] Shin H and Fan S H 2006 *Phys. Rev. Lett.* **96** 073907
[15] Yao J, Liu Z, Liu Y, Wang Y, Sun C, Bartal G, Stacy A M and Zhang X 2008 *Science* **321** 930
[16] Poddubny A, Iorsh I, Belov P and Kivshar Y 2013 *Nat. Photon.* **7** 948
[17] Liu Z W, Lee H, Xiong Y, Sun C and Zhang X 2007 *Science* **315** 1686
[18] Jacob Z, Alekseyev L V and Narimanov E 2006 *Opt. Express* **14** 8247
[19] Salandrino A and Engheta N 2006 *Phys. Rev. B* **74** 075103
[20] Govyadinov A A and Podolskiy V A 2006 *Phys. Rev. B* **73** 115108
[21] Wu G X and Hong M H 2021 *Opt. Express* **29** 23073
[22] Rho J, Ye Z L, Xiong Y, Yin X B, Liu Z W, Choi H, Bartal G and Zhang X 2010 *Nat. Commun.* **1** 143
[23] Lu D and Liu Z W 2012 *Nat. Commun.* **3** 887
[24] Ma C B and Liu Z W 2011 *Nanophotonics* **5** 051604
[25] Lemoult F, Fink M and Lerosey G 2012 *Nat. Commun.* **3** 889
[26] Zhou Y and Hong M 2021 *Microsc. Res. Tech.* **84** 2381
[27] Johannes B and Paul L 2022 *Opto-Electron Sci* **1** 210003
[28] Wang Z B, Guo W, Li L, Luk'yanchuk B, Khan A, Liu Z, Chen Z C and Hong M H 2011 *Nat. Commun.* **2** 218
[29] Mansfield S M and Kino G S 1990 *Appl. Phys. Lett.* **57** 2615
[30] Kim M S, Scharf T, Haq M T, Nakagawa W and Herzig H P 2011 *Opt. Lett.* **36** 3930
[31] Fan W, Yan B, Wang Z B and Wu L M 2016 *Sci. Adv.* **2** e1600901
[32] Chen L W, Zhou Y, Li Y and Hong M H 2019 *Appl. Phys. Rev.* **6** 021304
[33] Fletcher D A, Crozier K B, Guarini K W, Minne S C, Ginzton E L, Kino G S, Quate C F and Goodson K E 2001 *J. Microelectromech. Syst.* **10** 450
[34] Hao X, Kuang C F, Liu, Zhang H J and Li Y H 2011 *Appl. Phys. Lett.* **99** 203102
[35] Jiang W X, Qiu C W, Han T, Cheng Q, Ma H F, Zhang S and Cui T J 2013 *Adv. Mater.* **25** 6963
[36] Bogucki A, Zinkiewicz L, Grzeszczyk M and Kossacki P 2020 *Light Sci. Appl.* **9** 1
[37] Lin Z Y and Hong M H 2021 *Ultrafast Science* **2021** 9783514
[38] Gan Q, Song G and Chen L 2006 *Laser Phys. Lett.* **3** 278
[39] Zhan T R, Shi X, Dai Y Y, Liu X H and Zi J 2013 *J. Phys: Condens. Matter.* **25** 215301
[40] Pendry J B, Schurig D and Smith D R 2006 *Science* **312** 1780
[41] Leonhardt U 2006 *Science* **312** 1777
[42] Xu L and Chen H Y 2014 *Nat. Photon.* **9** 15
[43] Zhao P F, Cai G X and Chen H Y 2022 *Sci. Bull.* **67** 246
[44] Pendry J B 2003 *Opt. Express* **11** 755